JOURNAL OF AIRCRAFT
Vol. 36, No. 6, November–December 1999

Measurements of Unsteady Aeroelastic Model Deformation by Stereo Photogrammetry

Edward T. Schairer* and Lawrence A. Hand*
NASA Ames Research Center, Moffett Field, California 94035

Stereo photogrammetry measurements of the deformation of simple, flat-plate, clipped delta wings that were undergoing aeroelastic oscillations in transonic flow are described. The measurements were made in High Reynolds number Channel 2 at NASA Ames Research Center. Two types of aeroelastic responses were measured: 1) highly damped responses in which the tip of the model was deflected and then released at subcritical dynamic pressures; and 2) responses excited by perturbations in the flow as the dynamic pressure was slowly increased until the model became unstable. The model was imaged by three synchronized black-and-white video cameras, and the data were recorded on videotape. Correlated images from two of these cameras were used to estimate the space coordinates of reference marks on the model at each instant, and the motion of each mark was estimated by fitting the deflection data with a damped sinusoid. The resulting estimates of the frequency and damping of the first-bending-mode oscillations compared favorably with strain-gauge measurements. A large increase in the phase difference between motions of the leading and the trailing edges was observed just before the models became unstable.

Nomenclature

b = model span
c = distance from perspective center to image plane
c_l = local chord
f = frequency
k = reduced frequency $= \pi f c/U$
L_{1-11} = direct linear transformation coefficients
M = Mach number
m_{ij} = rotation matrix between image and space coordinate systems
p_∞ = freestream static pressure
q = dynamic pressure
t = time
U = freestream velocity
X, Y = image coordinates, pixels
X_p, Y_p = point in image plane that is closest to the perspective center
x = axial distance downstream from model root leading edge
x_0, y_0, z_0 = camera perspective center
y = spanwise distance outboard from model root
z = vertical distance above plane of wing
α = angle of attack
ζ = damping ratio $= 1/\sqrt{[(\omega/\eta)^2 + 1]}$
η = damping coefficient
$\theta_{c/4}$ = phase angle of vertical motion of local quarter chord, deg (zero when local quarter chord passes upward through $z = 0$)
λ = scale factor
ω = circular frequency

Subscripts

aero = aerodynamic
le = leading edge
te = trailing edge
$0.75c$ = three-quarter chord

Introduction

IN the past decade numerical methods have been developed for computing the aeroelastic responses of structures by use of computational fluid dynamics (CFD) to represent aerodynamic terms.[1] Only such methods can capture aeroelastic interactions in which nonlinear flow phenomena (e.g., shock waves, vortices, separated flow) play an important role. To test the accuracy of these methods, measurements are needed on flexible wind-tunnel models of unsteady aeroelastic deformation and unsteady pressure distributions. This need motivated a simple experiment at NASA Ames Research Center wherein two optical techniques for making these measurements were investigated: pressure-sensitive paint (PSP) for surface pressures and stereo photogrammetry for model deformation. The PSP measurements have already been reported[2]; this paper presents results of the photogrammetry measurements.

Photogrammetry is the science of determining spatial coordinates of an object from images of the object, usually acquired from two or more directions. It is a natural choice for measuring model deflections in experiments in which PSP is being used because many of the hardware (camera, framegrabber, etc.) and software (image acquisition and processing) requirements are the same for both techniques. For example, the inverse photogrammetry transformation—determining image coordinates from spatial coordinates—is now routinely used in PSP data reduction to locate in PSP images features of a model whose space coordinates are known (e.g., pressure taps or nodes of a numerical surface grid).[3] In addition, many lower-level image-processing operations (for example, locating targets in images) are required in both photogrammetry and PSP data reduction.

The first measurements of model deflection by photogrammetry were made in the NASA Langley Research Center 8-ft transonic pressure wind tunnel. They were motivated by the need to account for significant changes in shape of rigid models tested at high Reynolds numbers.[4] Subsequently, photogrammetry systems were developed for the National Transonic Facility,[5,6] culminating in a one-camera system with an emphasis on measuring wing twist.[7] Photogrammetry has also been applied in aeroelasticity research at NASA Langley in the Transonic Dynamics Tunnel, in which static deflections of a very flexible aeroelastic wing model were measured.[8] At NASA Ames Research Center, photogrammetry has

---

Presented as Paper 97-2217 at the AIAA 15th Applied Aerodynamics Conference, Atlanta, GA, 23–25 June 1997; received 17 August 1997; revision received 15 December 1998; accepted for publication 31 January 1999.

*Aerospace Engineer, Experimental Physics Branch.

been applied in two tests in the 80 × 120 ft wind tunnel: one in which the local angle of attack of a parafoil was measured,[9] and the other in which the positions of wingtip vortices from a fighter aircraft were measured.[10]

Most unsteady photogrammetry measurements in wind tunnels have involved tracking objects or particles. At Technion–Israel Institute of Technology, Seginer et al.[11] used photogrammetry to track the trajectory and the orientation of a free-flight, rigid model in a supersonic/transonic wind tunnel. Photogrammetry is also used in particle-tracking velocimetry to compute the trajectories of neutrally buoyant tracer particles in small-scale, incompressible flows.[12] The only published photogrammetry measurements of unsteady aeroelastic responses are from the Ames parafoil test, in which the unexpected collapse of the parafoil was documented. NASA Langley researchers have acquired images of unsteady model and model-support responses; however, these data have not been fully analyzed and remain unpublished.[*] Finally, in Russia, researchers at TsAGI have developed a one-video-camera photogrammetry system for measuring the deflection (flap, lead/lag, and pitch) of helicopter rotor blades in the rotating frame of reference.[13]

This paper describes an experiment in which the unsteady deformation of a simple, flat-plate, semispan model was measured in still air and in transonic flow by stereo photogrammetry. Results are shown for two types of responses: 1) highly damped responses at subcritical pressures in which the tip of the model was initially deflected and then released, and 2) increasingly large responses excited by perturbations in the flow as the pressure in the wind tunnel was slowly increased until the model became unstable.

Apparatus

Wind Tunnel and Test Section

The experiment was conducted in High Reynolds number Channel 2 at NASA Ames Research Center. This is a blowdown wind tunnel that operates at transonic speeds and at total pressures from 1 to 100 psia.[14] The test section for these experiments (Figs. 1 and 2) was 16 in. wide, 24 in. high, and approximately 8 ft long. All four walls were impermeable, straight, and rigid. The top and the bottom walls each diverged from the tunnel axis by 0.20 deg to compensate for the growth of wall boundary layers, and each had an 11 × 14 in. window (UV-transmitting Plexiglas, $\frac{3}{4}$ in. thick) centered at the model station. The semispan models were supported by a 16-in.-diam steel turntable that was mounted in one sidewall. Mach number in the test section was controlled by adjusting the height of a two-dimensional convergent–divergent choked nozzle ("speed flaps") downstream of the test section.

Models

Several identical models were tested. They were semispan clipped delta wings that were cut from flat 0.035-in.-thick cold-rolled steel plates (Figs. 3 and 4). The model thickness was a compromise between the need for stiffness (required for supporting lift loads at nonzero angles of attack, at which PSP measurements were made) and the need for low oscillation frequencies (required for reducing the frequency-response requirements of the pressure paint and for increasing the number of images per cycle). The models had no pressure taps, and their leading and trailing edges were blunt. An extension of the wing root of each model was clamped between stainless-steel blocks that fit in a slot in the turntable. The upper surfaces of the models were coated with PSP. Circular targets (approximately $\frac{1}{16}$ to $\frac{1}{8}$ in. in diameter) were applied in a regular pattern on top of the pressure paint with a permanent-ink felt-tip pen.

A finite-element structural analysis method[15] was used to estimate vibration modes (Fig. 4) and flutter pressures and frequencies. The p-k method[16] was used for the flutter analysis, and unsteady aerodynamics were represented by doublet lattices. The analysis predicted that, at $M = 0.85$, flutter occurs when the second mode becomes unstable at $q = 2.75$ psi.

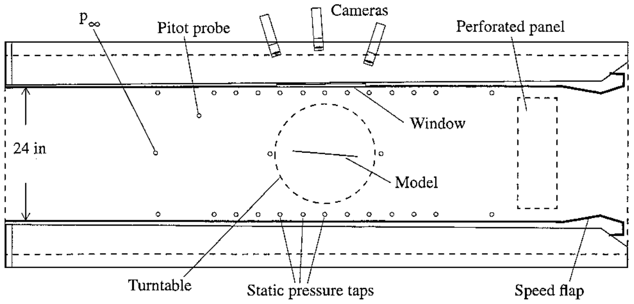

Fig. 1 Side view of test section.

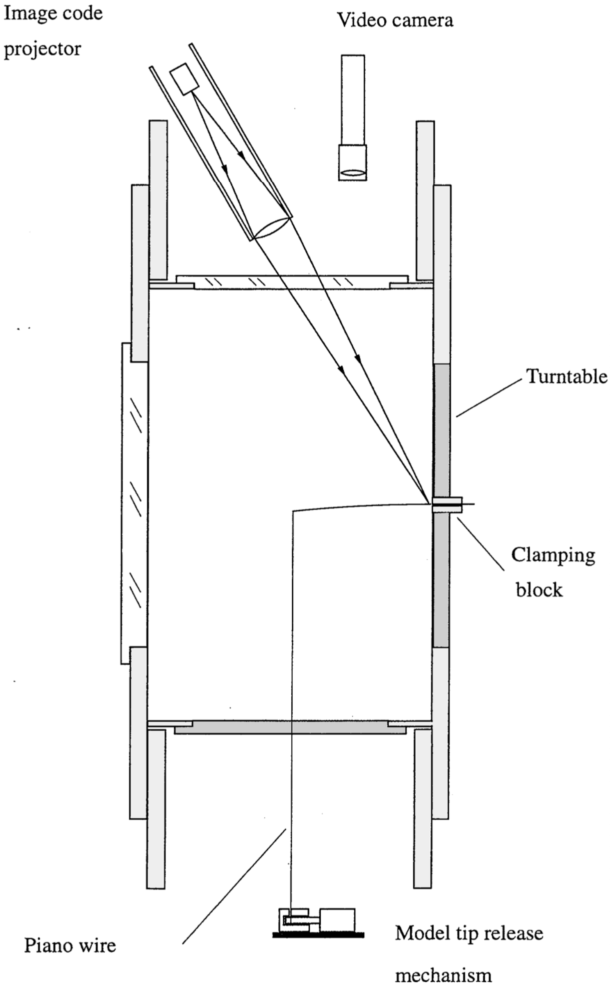

Fig. 2 Cross section of test section.

For several runs the tip of the model was deflected before the run and released after steady freestream conditions had been established. This was done by tying one end of a piece of 10-mil piano wire through a small hole in the wingtip and passing the other end through a small hole in the lower wall directly below the wingtip and looping it around the core of a solenoid (Fig. 2). The wingtip was released by energizing the solenoid, causing the core to retract out of the loop. The loop was too large to pass through the hole in the lower wall, so the slack in the wire between the wingtip and the loop bowed downstream during the run.

Cameras

The models were imaged through the window in the upper wall of the test section by three Pulnix 745-E black-and-white video cameras (Figs. 1–3). These cameras, which have a resolution of 768 × 493 pixels, an active pixel area of ~50%, and an 8.4 × 6.4 mm charge-coupled device (CCD), were chosen primarily because of

---

[*] Burner, A.W., NASA Langley Research Center, Langley, Virginia, private communication.

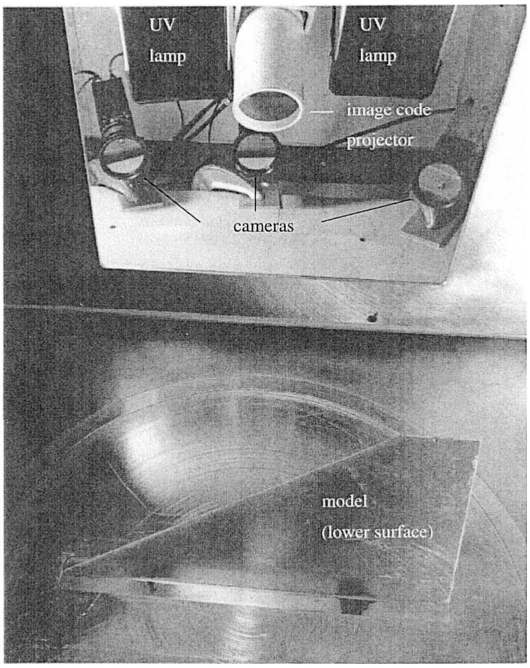

Fig. 3 Photograph of test section from below and outboard of wing tip.

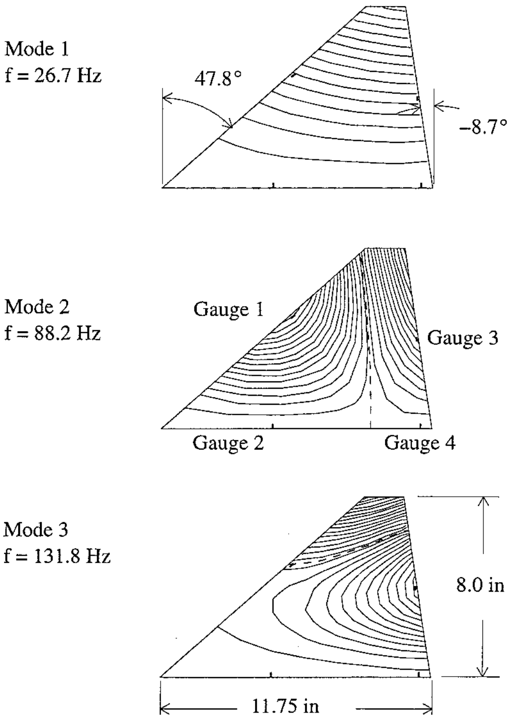

Fig. 4 Model geometry, vibration modes, and strain-gauge locations.

their sensitivity to low light levels (0.5 lux)—a prime requirement for making the PSP measurements. In addition, they were suitable for unsteady measurements because their integration times could be adjusted between $\frac{1}{60}$ and $\frac{1}{8000}$ s, and the exposure of all elements of the CCD was simultaneous. Their principal disadvantage in this application was their low imaging rate: they produced half an image (even or odd rows) every $\frac{1}{60}$ s and thus provided no more than one or two images per cycle of a model vibrating in the range 30–60 Hz.

Sensitivities of the cameras were doubled by switching them to field mode, in which pairs of adjacent rows are summed during readout. This enabled the cameras to produce a full image every $\frac{1}{60}$ s but cut their vertical spatial resolution in half.

The cameras were driven by, and thus synchronized to, a single external synchronization (sync) source (Leitch SPG-120N). They were positioned at three streamwise stations (Figs. 1 and 3) and were oriented with the rows (long dimension) of their CCD arrays in the streamwise direction. The cameras were located (Fig. 1) approximately 20 in. (1.7 root chords) above the model; the separation between the upstream and the downstream cameras was ~16 in. (1.36 root chords), and their optical axes formed an angle of ~35 deg. Each camera was equipped with a 12.5-mm focal-length, $\mathcal{F}/1.4$ lens and a bandpass interference filter (650 nm, required for PSP).

Lamps

The models were illuminated through the Plexiglas window in the top wall by two 250-W UV lamps (Electro-lite ELC 250, Fig. 3). This choice was dictated by the requirements of PSP. Steady, rather than flash, illumination was used because the pressure paint did not respond instantly to changing illumination.

Image Code Projector

Each video field was coded by projection of the display of a counter onto the model. The counter was positioned above the top window (Figs. 2 and 3) and had a 16-bit binary display formed by a single row of small, circular, red light-emitting diodes. For most cases, the counter was driven at 60 Hz by the vertical drive of the external sync source. In several cases the counter was synchronized to the strain-gauge data acquisition (see below) and thus was driven much faster (8 kHz). At 8 kHz and 60 Hz, the 16-bit counter could provide nonrepeating time codes for 8.192 and 1092 s, respectively. Coding the video data in this way made it possible to positively identify images from all three cameras that were recorded at the same time and to time correlate the video and the strain-gauge data.

Videotape Recorders and Framegrabber

The video data from all three cameras were recorded on videotape by three videotape recorders (VTRs) (Sony $\frac{3}{4}$-in. V-matic) and were retrieved frame by frame after the test. This was necessary because the framegrabber used (Data Translation DT2651, 8 bits, 512 × 480 pixels) could not acquire and store images at video frame rates. The vertical drive signal from the external sync source was also recorded on one audio track of each videotape. The external sync was turned on after the VTRs had begun recording, thereby establishing an unambiguous first pulse on each tape. The video data were retrieved when each VTR was connected in turn to the framegrabber in a minicomputer [Digital Equipment Corporation (DEC) MicroVAX]. The recorded external sync signal served as a frame counter during playback to allow retrieving a specific frame from each tape: Software was written to acquire an image from the framegrabber after a user-specified number of sync pulses had been read from the audio track by a DEC ADQ32 analog interface. The image code in each video field provided a check that the proper image had been retrieved. This procedure required replaying the tape from a point before the first sync pulse for every image retrieved.

Strain Gauges

Four strain gauges were epoxied to the lower surface of one model at the positions shown in Fig. 4. Gauges 1 and 3 were aligned with the wing's leading and trailing edges, respectively, and were placed for maximum sensitivity to the second and the third vibration modes, respectively. Gauges 2 and 4 were oriented perpendicular to the wing root. Gauge 4 was placed for maximum sensitivity to the first bending mode, and gauge 2 was placed so that differences in phase between its signal and that of gauge 4 could be used to infer second-mode vibration. Each gauge (1000 Ω, temperature compensated) was paired with a 1000-Ω fixed resistor and connected to a signal-conditioning amplifier to form an autobalancing Wheatstone bridge with one active arm. The outputs were low-pass filtered (400 Hz, −48 dB/octave), differentially multiplexed, sampled at 2 kHz each, and digitized by a data-acquisition board in a personal computer. The sampling was controlled by the onboard timer/counter, which, for some cases, was also used to drive the image code projector.

Pressure and Temperature Instruments

Pressures in the test section were measured by electronically scanned pressure transducers (PSI ESP-32, ±15 psid) that were calibrated before each run against a reference pressure transducer[17] (Datametrics Barocel). Flow temperature was measured by thermocouples in the settling chamber. Data acquisition was controlled by the MicroVAX computer. Each transducer, Barocel, and thermocouple was sampled at a rate of approximately 10 Hz.

Method

Theory

Spatial coordinates of reference points on the model were determined from video images with the direct linear transformation (DLT) formulation of the colinearity equations. The colinearity equations are the basis of photogrammetry and assume that a point in space and its image can be connected by a straight line that passes through the perspective center of the camera (Fig. 5). By this assumption, space and image coordinates are related by[18]

$$\begin{bmatrix} X - X_p \\ Y - Y_p \\ -c \end{bmatrix} = \lambda \begin{bmatrix} m_{11} & m_{12} & m_{13} \\ m_{21} & m_{22} & m_{23} \\ m_{31} & m_{32} & m_{33} \end{bmatrix} \begin{bmatrix} x - x_0 \\ y - y_0 \\ z - z_0 \end{bmatrix} \tag{1}$$

Dividing the first and second rows of Eq. (1) by the third yields

$$X - X_p = -\frac{c[m_{11}(x - x_0) + m_{12}(y - y_0) + m_{13}(z - z_0)]}{m_{31}(x - x_0) + m_{32}(y - y_0) + m_{33}(z - z_0)} \tag{2a}$$

$$Y - Y_p = -\frac{c[m_{21}(x - x_0) + m_{22}(y - y_0) + m_{23}(z - z_0)]}{m_{31}(x - x_0) + m_{32}(y - y_0) + m_{33}(z - z_0)} \tag{2b}$$

The terms that describe the camera (c, X_p, Y_p), its position (x_0, y_0, z_0), and its orientation (m_{ij}) can be collected into eleven coefficients (L_{1-11}) of the spatial coordinates:

$$X + \frac{L_1 x + L_2 y + L_3 z + L_4}{L_9 x + L_{10} y + L_{11} z + 1} = 0 \tag{3a}$$

$$Y + \frac{L_5 x + L_6 y + L_7 z + L_8}{L_9 x + L_{10} y + L_{11} z + 1} = 0 \tag{3b}$$

This is the DLT representation of the colinearity equations derived by Abdel-Aziz and Karara.[19] When these equations are applied to at least six noncoplanar points whose space and image coordinates are known (for example, by imaging a calibration object), it is possible to solve a least-squares problem for the eleven DLT coefficients. This approach is convenient because it requires no information about the camera or its position and orientation.

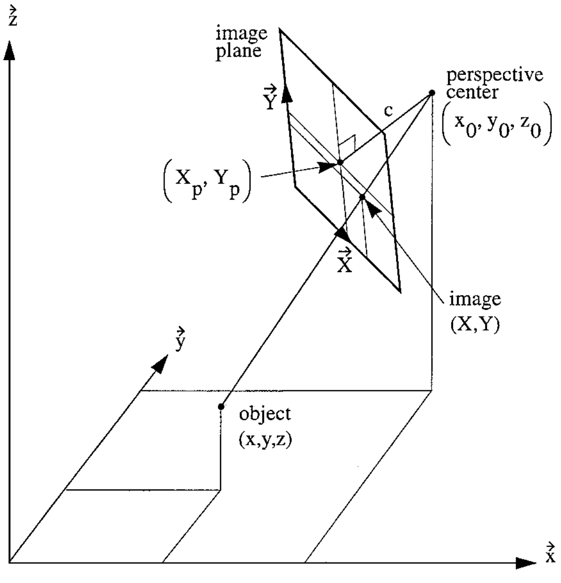

Fig. 5 Geometry describing colinearity condition.

Equations (3) uniquely relate each point in space to a point in the image plane of a given camera. The inverse transformation—from image to space coordinates—is not unique since each image point corresponds to a line of points in space. Therefore, without additional assumptions, images from at least two directions (i.e., from two cameras) are required for determining spatial coordinates from image coordinates. Each view contributes a pair of equations of the following form to a system that can be solved in a least-squares sense for the three unknown spatial coordinates:[4]

$$-(L_4 + X) = (L_1 + XL_9)x + (L_2 + XL_{10})y + (L_3 + XL_{11})z \tag{4a}$$

$$-(L_8 + Y) = (L_5 + YL_9)x + (L_6 + YL_{10})y + (L_7 + YL_{11})z \tag{4b}$$

Calibration

The DLT coefficients for the cameras were determined by installing a horizontal calibration plate in place of the model between runs. The position of the plate relative to the wind tunnel and the positions of targets on the plate were assumed to be known. Removable cylindrical pegs of various heights with targets at their centers were positioned in holes at known locations on the plate. They provided out-of-plane targets in the range $z/b = -0.14$ to $+0.125$. The plate was illuminated from above by white light and was imaged by all three cameras several times, each time with the pegs in a different configuration.

Locating Targets

At the scale of the images (approximately 40 pixels/in.) the targets were typically 3–5 pixels in diameter. Image coordinates of targets were determined by an automatic algorithm that sweeps through a rectangular window of pixels centered on the expected location of each target and defines the perimeter of groups of pixels with intensities lower than some threshold value. The image coordinates of each target are determined by computing the centroid of the group of subthreshold pixels within the perimeter, in which the weight given each pixel is proportional to the difference between its intensity and the threshold. The wingtip trailing edge was sometimes used as a target, in which case the analyst would interactively locate it with the computer's mouse-controlled cursor.

Accuracy

The accuracy of the photogrammetry measurements was estimated by applying the DLTs computed from one configuration of the calibration plate to images of the plate in a second configuration and then comparing the computed spatial coordinates of the targets with their known coordinates. The rms difference between computed and actual spatial coordinates was typically ~0.020 in. in each direction when images from only the upstream and the downstream cameras were used. Including images from the middle camera did not significantly improve the accuracy of the measurements. An image-coordinate change of one pixel in the streamwise direction (i.e., the direction between the cameras) resulted in a change in the vertical space coordinate of $\Delta z = 0.040$ in.; small changes in image coordinates in the spanwise direction (perpendicular to the line between the cameras) had almost no effect on the computed spatial coordinates. This numerically determined uncertainty is somewhat lower than that predicted with the simplified accuracy analysis of Meyn and Bennett,[9] which, for our geometry, predicts a variation of $\Delta z = 0.074$ in per streamwise pixel.

When the model was undergoing large-amplitude oscillations, the images of targets near the tip were blurred, and the uncertainty in locating them could be as high as 2–3 pixels. This corresponds to a spatial uncertainty of ~0.08–0.12 in. The uncertainty of the photogrammetry measurements also increased when the model deflection exceeded the range of vertical positions of targets on the calibration plate.

Curve-Fitting Vertical Deflection Data

The time history of the vertical displacement of each target on the model was estimated by fitting the photogrammetry deflection data with a damped sinusoid[20]:

$$z(t) = A_0 + (A_1 \cos \omega t + B_1 \sin \omega t)e^{-\eta t} \tag{5}$$

Where A_0, A_1, and B_1 are constants. The curve-fitting method fails when the frequency $f = 2\pi\omega$ is an integer multiple of the Nyquist frequency, i.e., half the video sampling rate or 30 Hz.

Strain Gauges

The spectral content of the strain-gauge signals was estimated by identifying peaks in the discrete Fourier transform of the digitized strain data after a cosine taper window had been applied to the first and the last 10% of the data record. The amplitude envelopes of tip-release transients were computed as the root sum square of the raw strain data and its Hilbert transform at each instant during the transient.[21] The damping was then determined by fitting a single exponential decay function to the amplitude envelope.

Results

Two sets of results are presented. The first set shows responses of a nonlifting wing ($\alpha = 0$ deg) to an initial tip deflection. Responses in still air (atmospheric pressure) and in transonic flow ($M = 0.85$, $q = 1.85$ psia) are compared. Frequencies and damping determined from the photogrammetry data are compared with strain-gauge measurements. The second set of data is for a nonlifting wing in transonic flow ($M = 0.85$) in which the tip of the model was unrestrained and the dynamic pressure was slowly ramped upward until the model became unstable. All photogrammetry measurements were based on images from the upstream and the downstream cameras only.

Responses of Wing to an Initial Tip Deflection: Still-Air vs Transonic

The wingtip was initially deflected downward ~1.25 in. ($z/b = -0.156$). Each strain gauge was sampled at 2 kHz, and 5 s of data were acquired, beginning ~1 s before the wingtip was released. Because of instrumentation problems, no useful strain-gauge data were obtained from gauge 4 for the still-air case or from gauge 3 for the wind-on case. For the still-air case, the camera shutters were set to $\frac{1}{1000}$ s, and the image code was incremented at the strain-gauge data sampling rate; for the wind-on case, the camera shutter speed was $\frac{1}{500}$ s, and the image code was incremented at 60 Hz by the external sync source.

Figure 6 compares raw strain-gauge and photogrammetry data for the still-air and wind-on cases. For the wind-on case, the strain data are from gauge 4, which yielded the cleanest signal for first-bending-mode motion. For the still-air case, however, the data presented are from gauge 2 because gauge 4 was not operational.

The photogrammetry data are for the trailing edge of the wingtip. Data acquired before the tip was released have been fit with a straight line, and the postrelease data have been fitted by a damped sine wave, as described in the preceding section. The time of tip release was estimated by extrapolating backward from the first postrelease data point to the first extremum of the damped sine wave. Two curve-fit solutions are shown for both the still-air and the wind-on cases, one with a frequency slightly above and the other slightly below the Nyquist frequency of the cameras (30 Hz). In both cases, one of these solutions was rejected because it was incompatible with the initial tip deflection. Other higher-frequency, curve-fit solutions were also possible; however, these were not consistent with the expected frequency of first-bending-mode oscillations (Fig. 4). The rms errors of the curve fits for the still-air and the wind-on cases were both approximately $\Delta z/b = 0.006$. Computed frequencies of all targets on the model agreed with each other to within 3%. The standard deviation of computed damping ratios among the targets was 0.0036.

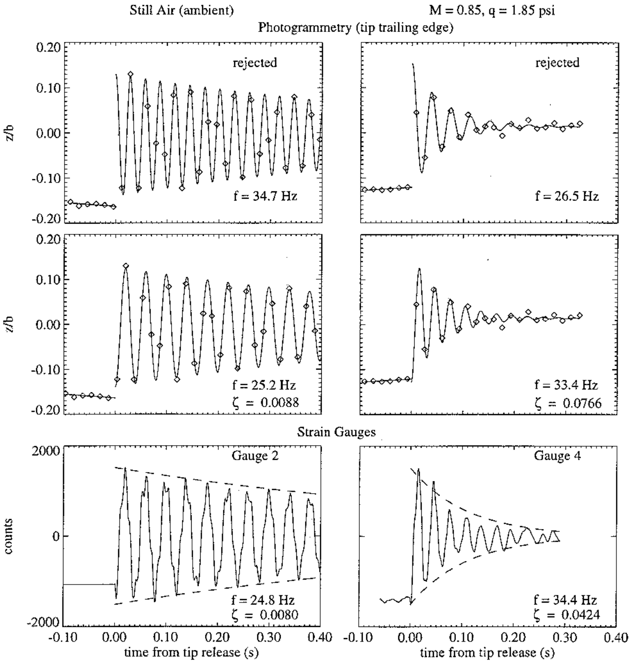

Fig. 6 Comparison of photogrammetry and strain-gauge measurements: still-air and wind-on responses to an initial tip deflection.

The response of the wing in the wind-on condition was much more highly damped than it was in still air, and the frequency of the first-bending-mode oscillation was somewhat higher. This was indicated by both the photogrammetry and the strain-gauge data (Fig. 6). The first-mode frequencies computed from the photogrammetry and strain data agree to within 3%, and, in still air, both are slightly lower than the computed first-mode natural frequency (Fig. 4). Damping ratios determined by the two experimental methods were in good agreement for the still-air case, but differed significantly for the wind-on case, in which the wing response was complicated by random flow perturbations. Note that first-mode damping was computed from raw data (both strain and photogrammetry), which included higher-order modes. The resulting error is small because of the dominance of the first mode.

Responses of Wing in Transonic Flow with Slowly Increasing (Ramped) Pressure

The pressure in the test section was initially ~0.7 psia, and the wingtip was unrestrained. Both video and pressure data were recorded as an upstream control valve was opened very slowly at a constant rate. No strain-gauge data were acquired. The upstream valve was abruptly closed when the model, as viewed on a video monitor, became unstable. The image code projector was driven at 60 Hz by the external sync source, and the camera shutters were set to $\frac{1}{1000}$ s.

The pressure in the test section increased slowly enough that, at any instant, the freestream conditions could be considered constant, i.e., the process was quasi steady. For example, near the end of the run the pressure changed at the rate of 0.3%/s, and the model oscillated at ~50 Hz, so the average pressure change per cycle was less than 0.01%.

After the test, 7 sets of 11 sequential video frames (22 images) were retrieved from videotape, beginning at a pressure at which sustained, low-amplitude vibrations were just beginning to appear and ending during tunnel shutdown. We correlated the pressure and the video data by observing in the record of each when tunnel shutdown occurred. Then, knowing 1) the time of each pressure sample, 2) the image code of each video field, and 3) the video frame rate, we were able to assign a pressure to each image.

Figure 7 presents images from the upstream and downstream cameras when the wingtip was near its maximum downward and upward deflections just before tunnel shutdown. The image code can be seen in the black rectangle protruding from the root. The wingtip is blurred in both tipdown images because of lack of depth

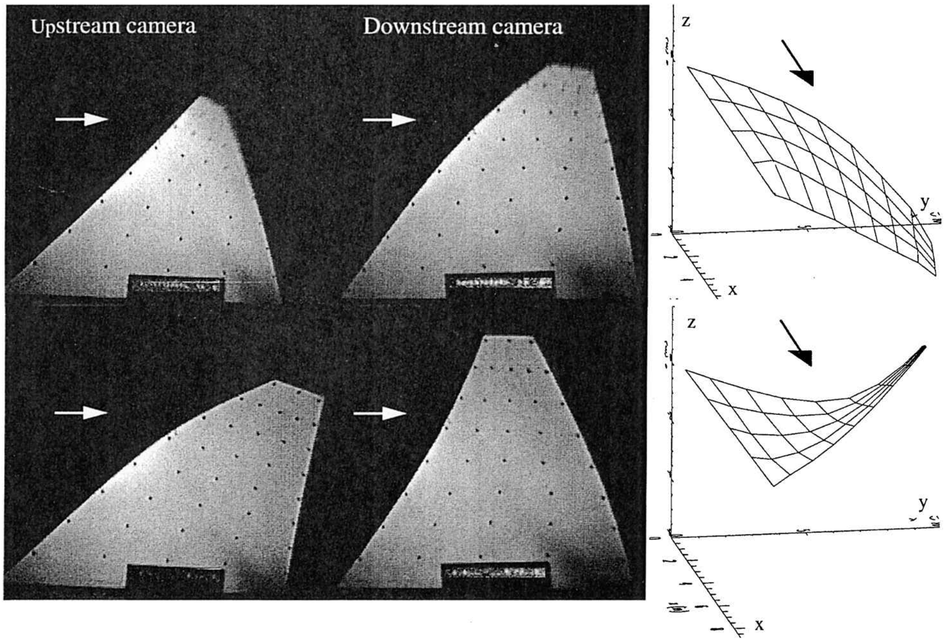

Fig. 7 Images from upstream and downstream cameras and computed deformation.

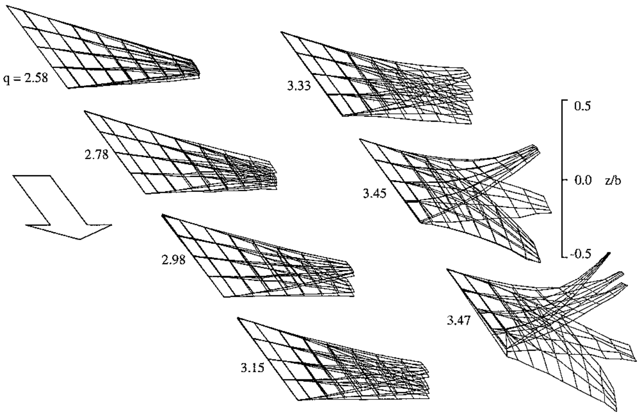

Fig. 8 Model deflection as dynamic pressure slowly increased (q in pounds per square inch).

of field. For each case, computed displacements of all the targets are presented as surface plots.

In Fig. 8, surface plots of the targets are shown for each of the seven sets of data before shutdown. For each set, deflections computed from five sequential images at $\frac{1}{60}$-s intervals are superimposed. The motion is clearly dominated by the first bending mode. Data at the highest pressure were recorded just before shutdown when the model was experiencing violent, large-amplitude oscillations.

Figure 9 presents the time history of the target at the wingtip trailing edge (visible in the two lower images of Fig. 7) derived from the last three sets of video data before shutdown. There was a marked increase in the amplitude of the motion and a slight increase in frequency as pressure increased. "Damping ratios" computed from the curve fits were nearly zero at all three conditions; however, because the motion was forced, this merely indicated quasi-steady conditions and was unrelated to the actual physical damping (thus the quotation marks). Just as for the case in which the wingtip was deflected and released, the photogrammetry data could be fit with sinusoids of different frequencies. For example, at $q = 3.45$ psi, solutions with frequencies of 9.7, 50.3, 69.7, and 110.3 Hz were possible (frequencies were equidistant above and below whole multiples of the sampling frequency). Because the vertical velocity (and thus blurring) of the wingtip was proportional to frequency, we selected the curve-fit frequencies that were most consistent with the observed blurring of the tip as the tip passed through $z = 0$ (i.e., where the tip velocity was maximum). We found that frequencies selected in this way were also most consistent with frequencies of the released-tip case (Fig. 6) and with the flutter frequency predicted by the finite-element structural analysis. The rms errors of the curve fits at all three pressures were approximately $\Delta z/b = 0.015$. At each pressure, computed frequencies of all the targets agreed with each other to within 1%, and the standard deviation of damping ratios among targets was typically 0.0015.

Figure 9 also illustrates the amplitudes and the phases of targets on the wing relative to the target at the wingtip trailing edge. Targets along the trailing edge were approximately in phase with each other at all pressures. In contrast, targets along the leading edge were progressively more out of phase with the tip the farther they were from it. This led to a phase difference between the leading and the trailing edges at each span station that increased dramatically at the highest pressure immediately before shutdown.

The amplitude contours measured at the lowest pressure were similar to the computed first-bending-mode contours (Fig. 4). The amplitude of the trailing edge was slightly greater than that of the leading edge, which indicates that the wing twisted as it bent. This twisting increased slightly as pressure increased. Together the phase and amplitude contours indicate an increase in wing twisting and an abrupt phase shift between bending and twisting motions immediately before shutdown.

Discussion

Comparison of Released-Wingtip and Ramped-Pressure Cases

The damping ratios determined from the released-wingtip and ramped-pressure cases are fundamentally different quantities. In the released-wingtip cases, the wing response is dominated by the transient because of the initial tip deflection, and the effects of excitation that are due to flow perturbations are small (zero for the still-air case) in comparison. Thus the decay of the transient is a good measure of the damping of the aeroelastic system. In the ramped-pressure case, however, the model is excited only by continual, random flow perturbations, and the amplitude envelope of the model's response is not, in general, indicative of the damping of the system. Other types of analyses, such as random decrement[22] or power spectral density,[23] are required for extracting system damping. The sampling rate of the video cameras was too low to allow applying these methods in the conventional manner.

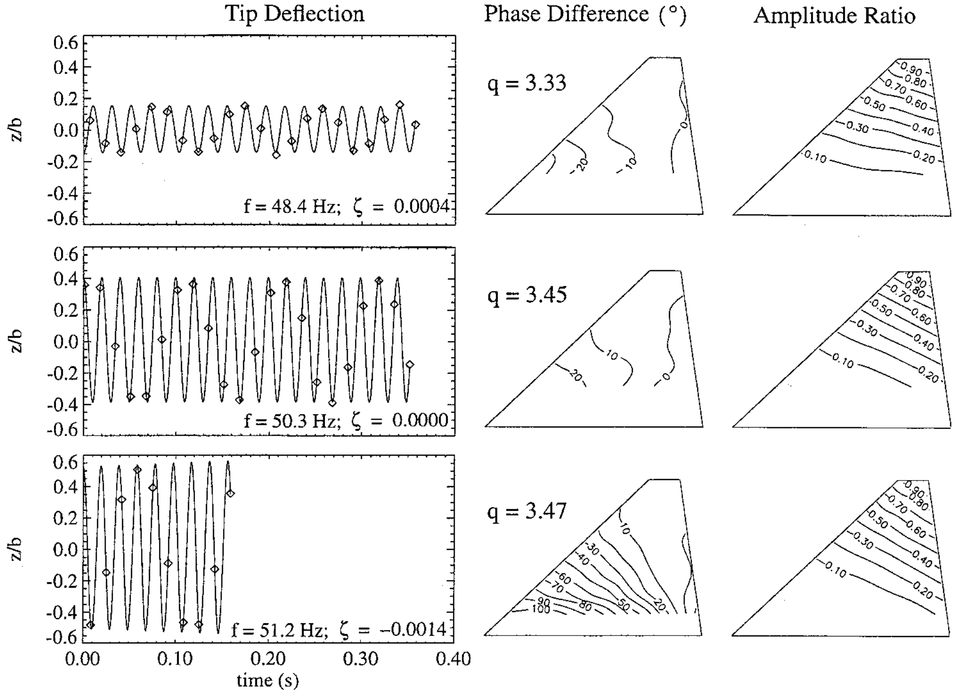

Fig. 9 Deflection of wingtip trailing edge, and phase difference and amplitude ratio with respect to tip trailing edge (q in pounds per square inch).

In the ramped-pressure case, the model became unstable at a considerably higher dynamic pressure (3.47 psi) than that predicted by the flutter analysis (2.75 psi). It is likely that in the experiment, in which deflections were very large, nonlinear structural and aerodynamic effects were important and may account for this difference. Properly accounting for these effects is what motivates the development of CFD-based aeroelasticity methods.

Aeroelastic Instability

The photogrammetry measurements show that, as the model approached the unstable condition, there was a shift in phase between local angle of attack(α_{aero}) and vertical motion near the wing root that caused the model to absorb energy from the flow. For linear, quasi-steady, two-dimensional flow, the center of pressure is at the local quarter chord, and the local aerodynamic angle of attack is given by[24]

$$\alpha_{\text{aero}} = \tan^{-1}\frac{z_{\text{le}} - z_{\text{te}}}{c} - \tan^{-1}\left(\frac{1}{U}\frac{\mathrm{d}}{\mathrm{d}t}z_{0.75c}\right)$$

In Fig. 10, α_{aero} at the tip ($y/b = 1.0$) and near the root ($y/b = 0.25$) are plotted vs the phase angle of the vertical motion of the quarter chord ($\theta_{c/4}$, $\theta_{c/4} = 0$ as the quarter chord passes upward through $z = 0$) for the last three conditions before shutdown. At the tip, α_{aero} is 180 deg out of phase with the quarter chord at all three conditions. Therefore, assuming lift is proportional to angle of attack, the lift at the tip is a springlike force, always acting to restore the tip to its undisturbed position. As with a spring, there is no net gain or loss of energy during each cycle. Near the root, the lift is also ~180 deg out of phase with the quarter chord at the two lower pressures; however, at the highest pressure, the relative phase of the lift has shifted so that it is almost 90 deg out of phase with the quarter chord and thus is nearly in phase with the vertical velocity of the quarter chord. Therefore the lift does work on the wing throughout each cycle. This is analogous to resonance of a forced mass-spring system.

The preceding argument assumes that the lift is in phase with angle of attack—something that, in general, is not true. Because no usable pressure-paint data were acquired during this run, the phase difference between lift and angle was not measured. However, at the reduced frequency of the condition shown ($k = 0.177$), it is likely that the lift lagged slightly behind the angle of attack.[24]

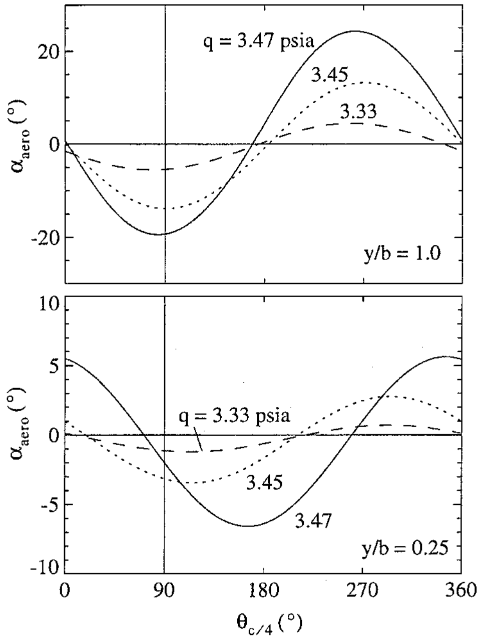

Fig. 10 Aerodynamic angle of attack vs quarter-chord phase angle.

Displacement Accuracy

The accuracy of the displacement measurements was limited by uncertainty in locating the images of targets on the wing. For the released-wingtip cases (Fig. 6), deflections were not large and thus image blurring was not a problem; however, especially in the still-air case, the images were so dim because of photodegradation of the pressure paint and short exposure times that targets on the wing could not be reliably located. Therefore the wingtip trailing edge—the most identifiable feature in the images—was used instead. The tip was located manually by the analyst, and the uncertainty could be as large as 2–3 pixels. The scatter in the still-air deflection measurements before tip release (Fig. 6), when the model was perfectly still, is an indication of this uncertainty.

The paint was significantly brighter and the targets were larger and more easily identifiable in the ramped-pressure case. Thus the most important source of displacement uncertainty was image blurring that was due to loss of depth of field, especially at the highest pressures when displacements were very large (Fig. 7). Uncertainty that was due to depth of field could have been decreased by stopping down the lenses; however, this would have required greater illumination.

Accuracy could also have been improved by 1) increasing the distance between the cameras (this would have required a larger window), 2) increasing the vertical range of targets on the calibration plate, 3) determining more precisely the spatial coordinates of targets on the calibration plate, and 4) applying corrections for lens distortion to the DLTs.[25]

Temporal Resolution

Our ability to reconstruct the time history of the model motion was limited by the low sampling rate of the video cameras compared with the model vibration frequencies. This introduced uncertainty that was due to aliasing and precluded measuring vibration frequencies higher than the first bending mode. It also made it impossible to measure highly damped responses of the model except by artificially creating very large initial perturbations. In several cases (not presented here), curve fitting the photogrammetry data was not possible because the model vibration frequency was too close to the Nyquist frequency. The temporal resolution could be improved for experiments in which the wingtip was deflected and released by combining images from several identical runs and releasing the wingtip at a different camera phase angle for each run. Clearly, however, it would be more desirable to use a high-speed camera.

Conclusions

Stereo photogrammetry was successfully used to measure the unsteady deformation of aeroelastic models. The first-mode amplitude, frequency, and damping of targets on the model were estimated by curve fitting the photogrammetry measurements with damped sinusoids. The accuracy of the displacement measurements was limited by uncertainty in locating the images of targets on the model. At each condition, frequencies of targets on the model agreed with each other and with independent strain-gauge measurements to within less than 3%. At each condition in which the wingtip was deflected and released, the standard deviation of computed damping ratios among the targets was less than 6% of the mean value. For the case in which the dynamic pressure in the tunnel slowly increased, the photogrammetry measurements revealed that the onset of aeroelastic instability coincided with an abrupt increase in the phase difference between the motions of the leading and the trailing edges near the wing root.

Acknowledgments

The authors thank Teresa Kaiser for performing the finite-element structural analyses of the models and Hoang Vu for help in preparing the experimental facility.

References

[1] Guruswamy, G. P., "Vortical Flow Computations on Swept Flexible Wings Using Navier–Stokes Equations," *AIAA Journal*, Vol. 28, No. 12, 1990, pp. 2077–2084.

[2] Schairer, E. T., and Hand, L. A., "Pressure-Sensitive Paint Measurements on Aeroelastic Wings in Transonic Flow," AIAA Paper 97-0389, Jan. 1997.

[3] McLachlan, B. G., and Bell, J. H., "Pressure-Sensitive Paint in Aerodynamic Testing," *Experimental Thermal and Fluid Science*, Vol. 10, No. 4, Oct. 1995, pp. 470–485.

[4] Brooks, J. D., and Beamish, J. K., "Measurements of Model Aeroelastic Deformations in the Wind Tunnel at Transonic Speeds Using Stereophotogrammetry," NASA TP 1010, Oct. 1977.

[5] Burner, A. W., Snow, W. L., and Goad, W. K., "Video Model Deformation System for the National Transonic Facility," NASA TM 85681, Aug. 1983.

[6] Burner, A. W., Snow, W. L., Goad, W. K., and Childers, B. A., "A Digital Video Model Deformation System," International Congress on Instrumentation in Aerospace Simulation Facilities, College of William and Mary, Williamsburg, VA, June 1987.

[7] Burner, A. W., Wahls, R. A., and Goad, W. K., "Wing Twist Measurements at the National Transonic Facility," NASA TM 110229, Feb. 1996.

[8] Byrdsong, T. A., Adams, R. R., and Sandford, M. C., "Close-Range Photogrammetric Measurement of Static Deflections for an Aeroelastic Supercritical Wing," NASA TM 4194, Dec. 1990.

[9] Meyn, L., and Bennett, M., "A Two Camera Video Imaging System with Application to Parafoil Angle of Attack Measurements," AIAA Paper 91-0673, Jan. 1991.

[10] Meyn, L. A., and Bennett, M. S., "Application of a Two Camera Video Imaging System to Three-Dimension Vortex Tracking in the 80- by 120-Foot Wind Tunnel," AIAA Paper 93-3439, Aug. 1993.

[11] Seginer, A., Kadushin, I., and Etrog, U., "An Improved Method of Wind Tunnel Free Flight Data Acquisition," International Congress on Instrumentation in Aerospace Simulation Facilities, Ottawa, Canada, Sept. 1975.

[12] Maas, H. G., Gruen, A., and Papantoniou, D., "Particle Tracking Velocimetry in Three-Dimensional Flows," *Experiments in Fluids,* Vol. 15, No. 2, 1993, pp. 133–146.

[13] Fonov, S. G., Kulesh, V. P., Tarazov, N. T., and Bosnyakov, S. M., "Preliminary Design and Testing of the Laboratory System to Measure Rotor Blade Deflections," European Research Office of the U.S. Army Contract N68171-94-C-9137, June 1995.

[14] McDevitt, J. B., Polek, T. E., and Hand, L. A., "A New Facility and Technique for Two-Dimensional Aerodynamic Testing," *Journal of Aircraft*, Vol. 20, No. 6, 1983, pp. 543–551.

[15] *MSC/NASTRAN Handbook for Aeroelastic Analysis*, Vol. 1 MSC/NASTRAN Ver. 65, MacNeal-Schwendler Corp., Los Angeles.

[16] Hassig, H. J., "An Approximate True Damping Solution of the Flutter Equation by Determinant Iteration," *Journal of Aircraft*, Vol. 8, No. 11, 1971, pp. 885–889.

[17] Olsen, M. E., and Seegmiller, H. L., "Low Aspect Ratio Wing Code Validation Experiment," *AIAA Journal*, Vol. 31, No. 10, 1993, pp. 1744–1752.

[18] Marzan, G. T., and Karara, H. M., "Rational Design for Close-Range Photogrammetry," PB-252447/8 UILU-ENG-76-2001, Univ. of Illinois, Urbana, IL, Jan. 1976.

[19] Abdel-Aziz, Y. I., and Karara, H. M., "Direct Linear Transformation from Comparator Coordinates into Object-Space Coordinates," *Proceedings of the Symposium on Close-Range Photogrammetry*, American Society of Photogrammetry, Urbana, IL, Jan. 1971.

[20] Bennett, R. M., and Desmarais, R. N., "Curve Fitting of Aeroelastic Transient Response Data with Exponential Functions," *Flutter Testing Techniques*, NASA Symposium on Flutter Testing Techniques, NASA SP-415, 1975, pp. 43–58.

[21] Deutsch, R., *Nonlinear Transformations of Random Processes*, Prentice–Hall, Englewood Cliffs, NJ, 1962, pp. 3–5.

[22] Cole, H. A., "On-Line Failure Detection and Damping Measurement of Aerospace Structures by Random Decrement Signatures," NASA CR-2205, March 1973.

[23] Ruhlin, C. L., Watson, J. J., Ricketts, R. H., and Doggett, R. V., "Evaluation of Four Subcritical Response Methods for On-Line Prediction of Flutter Onset in Wind Tunnel Tests," *Journal of Aircraft*, Vol. 20, No. 10, 1983, pp. 835–840.

[24] Fung, Y. C., *An Introduction to the Theory of Aeroelasticity*, Dover, New York, 1969, pp. 191–193.

[25] Karara, H. M., and Abdel-Aziz, Y. I., "Accuracy Aspects of Non-Metric Imageries," *Photogrammetric Engineering*, Vol. 40, No. 7, 1974, pp. 1107–1117.